IFASD 2015
International Forum on Aeroelasticity and Structural Dynamics
June 28 — July 02, 2015 ▲ Saint Petersburg, Russia

USING 2D-PIV MEASUREMENTS TO COMPUTE UNSTEADY AERODYNAMIC LOADS ON A FLAT PLATE AT HIGH ANGLE OF ATTACK

Amandine Guissart[1], Luis P. Bernal[2], Grigorios Dimitriadis[1], and Vincent E. Terrapon*[1]

[1]Department of Aerospace and Mechanical Engineering, University of Liege,
Quartier Polytech 1, 9 Allée de la Découverte, B52/3, 4000 Liège, Belgium
* Corresponding author: vincent.terrapon@ulg.ac.be

[2]Department of Aerospace Engineering, University of Michigan
3048 FXB, Ann Arbor, MI 48109-2140, USA

Keywords: Indirect load calculation, control volume approach, PIV, flat plate, unsteady flow.

Abstract: This work exposes and discusses results obtained for aerodynamic forces using an indirect calculation based on Particle Image Velocimetry (PIV) measurements. The methodology used is based on the integral formulation of the Navier-Stokes equations and is applied to spatio-temporal data for different flows around a plate with a 16:1 chord-to-thickness ratio at high angle of attack. Experimental data are obtained in a water channel for both a static and a pitching plate. In addition to PIV data, direct measurements of aerodynamic loads are carried out to assess the quality of the indirect calculation. It is demonstrated that this indirect method is able to compute the mean and the temporal evolution of the lift and drag coefficients with a reasonable accuracy. It is also shown that the noise sensitivity of the method can be partly alleviated through the use of Dynamic Mode Decomposition (DMD) as a pre-processing step to smooth the spatio-temporal data.

1 INTRODUCTION AND MOTIVATION

The direct measurement of aerodynamic loads with force balance can become challenging when the forces are small or when the body is moving. Moreover, the knowledge of sectional rather than global loads can be of interest to study the physical mechanisms underlying the generation of aerodynamic forces. In those cases, an interesting alternative to direct force measurement is the use of Particle Image Velocimetry (PIV) velocity fields to indirectly obtain the aerodynamic coefficients.

The different existing methods are all based on a control volume approach, or, in a two-dimensional case as in the present work, on a control surface approach. The traditional method consists in applying the integral form of the momentum equations to the control surface surrounding the geometry of interest. This requires both contour and surface integrals of the velocity and pressure fields, as described in section 2. Because PIV data do not provide the pressure, it needs to be computed from the velocity field. Moreover, the treatment of time derivatives in the vicinity of moving geometries can be challenging. An alternative approach has been proposed by Noca [1], in which the integral Navier-Stokes equations are rewritten such that only contour integrals are required. Additionally, the

pressure can be completely eliminated. Despite the clear advantages of Noca's method, it has been shown that the direct application of the integral momentum conservation leads to better results for separated turbulent flows [2].

In this work the traditional methodology is applied to spatio-temporal data obtained for the flow around a static or pitching plate. Although this approach is outwardly simple, several challenges must be overcome to ensure accurate results. First, the velocity typically cannot be measured in shadow regions inherent to most PIV setups, thus preventing the straightforward application of the control volume approach. Different strategies are possible to access the missing information. For instance, the illumination of the shadow regions can be achieved by modifying the PIV setup, such as through the addition of mirrors reflecting the laser beam. As this is not possible in the context of this work, the missing data points are found by leveraging the symmetry of the problem. Specifically, PIV measurements are conducted with both positive and corresponding negative angles of attack to obtain velocity fields on the two sides of the plate. The two sets of resulting velocity fields are then averaged and stitched together.

As mentioned above, another challenge of the method stems from the fact that PIV measurements do not provide the pressure field. Therefore, it must be indirectly determined from the velocity field. This can be achieved by either solving the pressure Poisson equation or integrating the pressure gradients, which are in turn calculated from the velocity field through the Navier-Stokes equations. The latter approach is used in the present work. Unfortunately, the integration of the pressure gradient along the contour of the control surface is very noise sensitive, which can lead to large errors in the computed aerodynamic forces. To overcome this problem, it is proposed to apply the Dynamic Mode Decomposition (DMD) [3] to decrease the noise level by selecting a small number of modes representative of the dynamics. Finally, the results quality is also affected by different parameters such as the spatio-temporal resolution, the location and size of the control surface (and thus of the PIV window), or the flow type.

These different aspects are investigated through the application of the method to the flow around a flat plate in different configurations. A static plate at different angles of attack is first considered. In a second step, different pitching motions are imposed. The predictions of aerodynamic forces by the indirect method are then assessed by comparison with results obtained from direct measurements.

The paper is organized as follows. Section 2 summarizes the mathematical background of the indirect calculation method and its implementation. It also discusses the different sources of error and proposes some improvement strategies. Section 3 describes the specific application considered and the experimental procedure. The results of the indirect load calculations and the comparison with direct measurements are then shown and discussed in section 4. Finally, conclusions and future work are presented in section 5.

2 METHODOLOGY

This section explains the mathematical background and the implementation of the indirect aerodynamic load calculation. It also shows how the pressure calculation can be corrected and how the Dynamic Mode Decomposition (DMD) can help improving the results.

2.1 Mathematical background

The indirect calculation of the aerodynamic forces is based on the integral form of the Navier-Stokes equations. As the velocity field is obtained from 2D-PIV measurements at low Mach number, only the two-dimensional incompressible case is considered. The aerodynamic force vector F_i can then be expressed as

$$\overline{F}_i = -\int_{\mathcal{S}} \rho \partial_t \overline{u}_i \, \mathrm{d}\mathcal{S} - \int_{\mathcal{C}} (\rho \overline{u}_i \overline{u}_j n_j - \overline{\tau}_{ij} n_j) \, \mathrm{d}\mathcal{C} - \int_{\mathcal{C}} \overline{p} n_i \, \mathrm{d}\mathcal{C} - \int_{\mathcal{C}} \rho \overline{u'_i u'_j} n_j \, \mathrm{d}\mathcal{C} \,, \qquad (1)$$

where ρ is the constant density, u_i the velocity vector, p the pressure and τ_{ij} the viscous stress tensor. The above expression contains both surface integrals over the control surface $\mathcal{S}$ surrounding the geometry of interest and closed-path integrals along the contour $\mathcal{C}$ of $\mathcal{S}$. The vector n_i represents the unit outward vector normal to the contour. A schematics of the configuration is shown in Fig. 1. Since the flow of interest is turbulent, only averaged quantities are considered (denoted by $\overline{\cdot}$). The last term on the right-hand side of Eq. (1) corresponds to the Reynolds stress tensor (where $\cdot'$ denotes fluctuations around the mean), which originates from the averaging of the nonlinear convective term. Since the flow is inherently unsteady but statistically periodic, the averaging operation does not correspond to a time average but to a phase average hereafter, unless specifically mentioned. Note that, except for the time derivative of the velocity, all integrals are closed-path integrals along the contour $\mathcal{C}$. In particular, this means that the viscous stress, the Reynolds stress and the pressure need only to be known on $\mathcal{C}$.

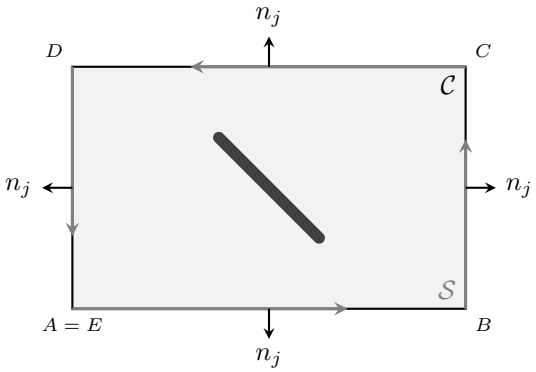

Figure 1: Schematic view of the control surface $\mathcal{S}$ and its contour $\mathcal{C}$ around the geometry of interest.

Each term in the above expression can be calculated from the velocity fields u_i obtained from PIV measurements. In particular, the averaged viscous stress tensor $\overline{\tau}_{ij}$ is computed from the averaged velocity gradients

$$\overline{\tau}_{ij} = \mu \left(\partial_i \overline{u}_j + \partial_j \overline{u}_i \right) \,, \qquad (2)$$

where the dynamic viscosity μ is constant. The averaged pressure field $\overline{p}$ is generally unknown but can also be derived from the averaged velocity field. Two approaches can be considered [4], both based on the knowledge of the averaged pressure derivatives calculated using the averaged Navier-Stokes equations:

$$\partial_i \overline{p} = -\rho \partial_t \overline{u}_i - \rho \overline{u}_j \partial_j \overline{u}_i + \mu \partial^2_{jj} \overline{u}_i - \partial_j \overline{u'_i u'_j}. \qquad (3)$$

The first option is to solve the Poisson equation obtained by taking the divergence of Eq. (3). Boundary conditions of Neumann type can be applied using Eq. (3). The second

option consists in integrating along $\mathcal{C}$ the component of the pressure gradient $\partial_i \overline{p}$ that is tangential to the contour. Since the integral is along a closed path, the accuracy of the pressure calculation can be partially assessed by comparing the pressure at points A and E in Fig. 1, which should be identical. Because the use of the pressure Poisson equation increases the computational time without improving results significantly [2], the second option has been chosen here.

2.2 Implementation

Eqs. (1)-(3) must be discretized in order to be applied to discrete PIV data. Spatial derivatives appearing in Eqs. (2) and (3) are only required along the contour $\mathcal{C}$. They are calculated using central finite difference schemes of fourth order for the first spatial derivatives and of second order for the second spatial derivatives. Temporal derivatives $\partial_t \overline{u}_i$ appear in Eqs. (1) and (3) and must be integrated over the entire control surface $\mathcal{S}$ (except in the body). These time derivatives are computed with a second order central scheme.

The averaged pressure is calculated by integrating the averaged tangential pressure gradient obtained from Eq. (3) along the closed path $\mathcal{C}$ as illustrated in Fig. 1. The integration path starts at point A where the pressure is supposed to be $\overline{p}_{init}$ and goes along $\mathcal{C}$ counterclockwise until point $E = A$. For each of the N points, a relation between the pressure and its derivative can be written using a finite difference scheme. To avoid an odd-even decoupling, a non-symmetric third order scheme is used for all points except the corners A, B, C, D and E, where a third order forward/backward scheme is used. This discretization can be expressed as a system of N equations that is solved for the N unknown pressure values.

Finally, the aerodynamic force can be estimated by integrating the different terms in Eq. (1) on the contour $\mathcal{C}$ and surface $\mathcal{S}$. The trapezoidal rule is used to perform these integrations.

2.3 Improvements

The averaged pressure computation is very noise sensitive and can lead to large errors in the resulting aerodynamic loads. As shown by Eq. (3), the averaged pressure gradient is the sum of first and second derivatives of the averaged velocity and its fluctuations. Thus, any noise existing in those quantities is amplified by the derivation, which leads to large errors during the integration process. Moreover, these errors accumulate along the integration path.

Results can be greatly improved through pre- and postprocessing. First, the noise in averaged velocity fields and its fluctuations can be greatly reduced by the use of DMD. This technique consists in decomposing the spatio-temporal data into spatial modes $\boldsymbol{\phi}_i$ oscillating at a single complex frequency λ_i and their corresponding initial amplitude a_i. The original data $\mathbf{f}(x, y, t)$ can thus be written as

$$\mathbf{f}(x, y, t) = \sum_{k=1}^{K} a_k \boldsymbol{\phi}_k (x, y) \exp(\lambda_k t), \tag{4}$$

where K is the total number of modes that depend on the number of time snapshots used in the decomposition. To decrease the noise in $\overline{u}_i$ and $\overline{u'_i u'_j}$, these quantities are first decomposed using DMD [3]. The modes are then sorted with respect to their initial amplitude a_k and only the first modes are used to reconstruct the fields. In other words, the sum in Eq. 4 is truncated, keeping only the most significant modes. The reconstructed fields are therefore only an approximation of the initial fields. They are used here to compute the aerodynamic coefficients. The accuracy of this reconstruction depends not only on the number of modes used but also on the complexity of the initial data. As the flow considered here is expected to be periodic with a few dominating frequencies/modes corresponding to the shedding/pitching frequency and its harmonics, a few modes should be sufficient to obtain a good approximation. Note that by definition, DMD is applied to unsteady fields. Therefore, this filtering step is not applicable in the context of the static plate considered in the following since only the time-averaged velocity is available.

Additionally, the errors generated by the pressure integration can be partially corrected. Since the integration path is closed, the averaged pressure computed at the last point E should be equal to the initial value at point A, i.e., $\overline{p}_E = \overline{p}_A = \overline{p}_{init}$. Any discrepancy corresponds to an integration error $\varepsilon_{\overline{p}} = \overline{p}_A - \overline{p}_E$ that can be used to improve the results. The proposed approach relies on a few assumptions. It seems reasonable to consider that most of the error is generated in the wake (edge $B - C$ in Fig. 1), where spatial variations of the velocity and pressure are the largest. This is therefore the region where the pressure gradient integration is numerically the most challenging. Assuming that the error is generated only along $B - C$ and then propagated along $C - D - E$, a correction can be done. Specifically, the error $\varepsilon_{\overline{p}}$ is simply removed from the computed value $\overline{p}$ along edges $C - D - E$. For the edge located in the wake, it is assumed that the error $\varepsilon_{\overline{p}}$ increases linearly from B to C. The pressure is corrected accordingly.

Finally, results have shown that the choice of the control surface can have a significant impact on the predictions. In order to reduce this sensitivity, the aerodynamic coefficients are computed here using different control surfaces $\mathcal{S}$ and are then ensemble averaged to obtain their final value. The standard deviation is also reported to highlight the sensitivity of the method to the choice of the control surface.

3 FLOW CONFIGURATIONS AND EXPERIMENTAL SETUP

The indirect force measurement described above is applied to three different cases for the unsteady flow around a plate. As large angles of attack are considered, the flow is massively separated and unsteady, which represents a major challenge for the method. The plate has a 16:1 chord-to-thickness ratio and its leading and trailing edges are rounded. The chord itself has dimension $c = 7.6$cm. The three cases and their specificities are first discussed. In a second step, the experimental setup is described.

3.1 Description of the different cases

The first case corresponds to a static plate at two different angles of attack (AOA), i.e., 30° and 45°, and a Reynolds number $\mathrm{Re} = U_\infty c/\nu = 4 \cdot 10^4$, where U_∞ is the freestream velocity, and ν the kinematic viscosity. As the shedding frequency is unknown, the PIV system cannot be synchronized with the periodic flow dynamics. Moreover, the sampling frequency of the PIV system is too low to ensure a sufficient resolution of a single period.

This precludes a phase averaging of the flow fields. Therefore, only the mean flow is considered here. The objective is to assess whether the indirect force calculation is able to predict the mean aerodynamic coefficients based on the mean velocity field. More specifically, the averaging operation in Eq. (1) can be understood as a time average in this particular case. As a consequence, the velocity time derivative vanishes and only contour integrals must be performed.

The second case attempts to alleviate this issue by forcing the periodic shedding at a given frequency. In particular, a sinusoidal pitching motion $\alpha = \overline{\alpha} + \Delta\alpha \sin(2\pi f t)$ with a very small amplitude $\Delta\alpha$ is imposed around the mean angle of attack $\overline{\alpha}$. The pivot axis is located at the center of the plate, i.e., at mid-chord. The frequency is chosen to be as close as possible to the shedding frequency of the static plate. This allows to synchronize the PIV system with the forcing frequency without strong alteration of the natural flow dynamics compared to a static plate [5]. PIV velocity fields can therefore be obtained at selected phases and a phase averaging can be applied to analyze the time behavior of the velocity field and aerodynamic forces. Here again, the Reynolds number is $\mathrm{Re} = 4 \cdot 10^4$, and both 30° and 45° are used as mean angles of attack. The corresponding amplitudes $\Delta\alpha$ are 0.77° and 1.33°, respectively. In both cases, the non-dimensional frequency, i.e., the Strouhal number, $\mathrm{St} = fc \sin\overline{\alpha}/U_\infty$ is 0.155, where f is the forcing frequency.

The third case also considers a forced pitching motion, but this time with a large amplitude. The objective is to assess the ability of the indirect method to deal with moving bodies. For this case, the large amplitude motion is characterized by a mean angle of attack $\overline{\alpha} = 0$ and an amplitude $\Delta\alpha = 30°$. The reduced frequency $k = \pi f c/U_\infty$ is 0.2 corresponding to the maximal reduced frequency studied in [6]. The pivot axis is again at mid-chord and for this third case, the Reynolds number is $\mathrm{Re} = 2 \cdot 10^4$.

3.2 Experimental setup

The different experimental measurements are conducted in a low turbulence free surface water channel facility at the University of Michigan [7] shown in Fig. 2. The freestream velocity ranges from 5cm/s to 55cm/s with a turbulence intensity of about 1%. The channel test cross-section has dimensions 61cm × 61cm as shown in Fig. 3, which corresponds to $8c \times 8c$. The model is mounted vertically and the immersed span corresponds to $7.6c$. The distance between the model and the bottom wall of the test section is about $0.04c$ to minimize three-dimensional effects. The two freestream velocities used here are 26cm/s and 52cm/s, which corresponds to $\mathrm{Re} = 2 \cdot 10^4$ and $4 \cdot 10^4$, respectively.

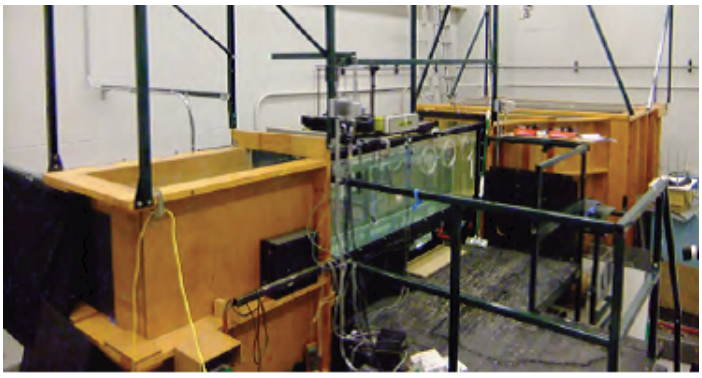

Figure 2: Overview of the water channel facility at the University of Michigan [7].

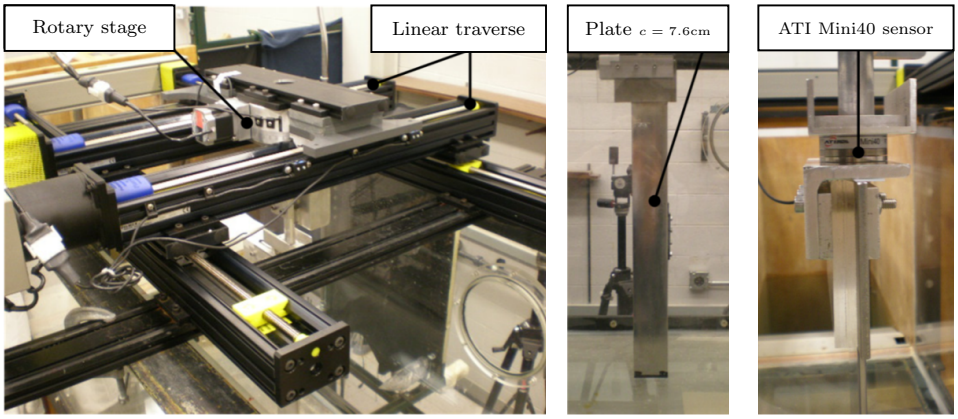

(a) Mounting in the water channel facility [8]

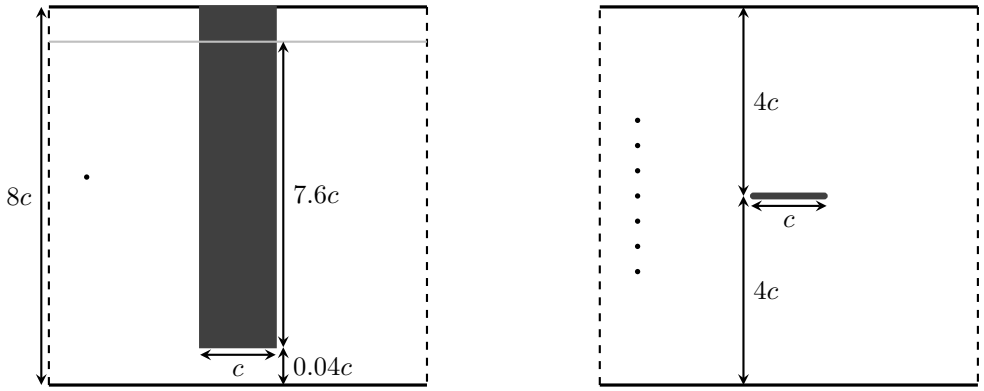

(b) Side view (c) Bottom view

Figure 3: Pictures and schematic view of the plate mounted in the water channel. The seven small discs represent the location of the dye rake.

Unsteady velocity fields are obtained through PIV measurements. The water channel is seeded with 3μm titanium dioxide particles and a plane near mid-span is illuminated on one side of the plate by a double-pulsed Nd-YAG laser (Spectra Physics PIV 300). Images are acquired by a digital camera (Cooke Corp. PCO.4000) equipped with Micro-Nikkor $105-$mm lenses which leads to magnification of approximately 18pixels/mm. The maximum acquisition frequency is 1Hz, which precludes the acquisition of more than one image per period.

Images are post-processed using an in-house code. The particle displacement, and thus the velocity, are determined in multi-passes using cross-correlation analysis. The first low-resolution and second high-resolution passes are performed using an interrogation window size of 64×64pixels and 32×32pixels, respectively. Two filters are then applied to remove outliers; a median filter based on spatially adjacent values and a $3-\sigma$ filter based on a pre-computed mean and standard deviation at one particular point. After post-processing, data are obtained on a 16 pixels spacing cartesian grid. It consists of about 225×200 points for a size of about $2.6c \times 2.3c$. The location of the window with respect to the plate is shown in Fig. 4.

For the first case, a series of 200 snapshots are taken at a frequency lower than the shedding frequency. As these images do not correspond to a specific phase, the velocity fields are averaged to obtain the mean flow, as explained above. For the second and third cases, the pitching motion is imposed by a rotary stage (Velmex B4872TS Rotary Table).

The laser pulses are then synchronized with the kinematics in order to acquire data at a specific phase for phase-averaging. 200 PIV images are collected for one given phase. The experiment is then repeated for subsequent values of the phase, up to a total of 20 phases uniformly distributed within the pitching period.

As previously mentioned, part of the plate is in the shadow region. To obtain the velocity field in that region, the experiment is repeated with the plate mounted symmetrically with respect to the freestream direction. Note that for the third case, the information on one side is sufficient as the pitching motion is symmetrical with respect to the freestream direction: a phase shift of half a period provides the corresponding flow field on the other side. The two sets of results are then stitched together. This step is of primary importance because of its large impact on the indirect forces calculation. It is performed on the mean and fluctuation of the velocity field obtained after application of the PIV algorithm and (phase or time) averaging. Since points are missing in the shadow region only, overlap regions exist between the images obtained for the two sides. These overlap regions are used to align the two sets of images. Despite this geometric overlap, the data usually do not match exactly. The two sets of data are thus stitched together based on a weighted-average in order to avoid discontinuities in the global velocity fields.

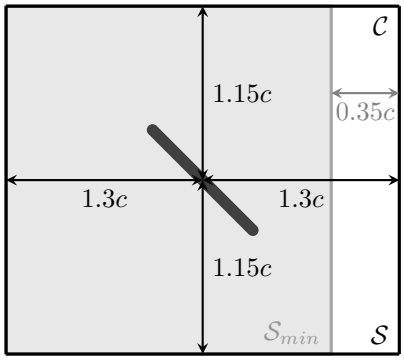

Figure 4: Schematic view of the control surface location with respect to the plate.

In addition to PIV measurements, aerodynamic loads are also directly measured to allow comparison with the indirect force calculation. A six component ATI Mini 40 forces/torques transducer attached as depicted in Fig. 3a is used for that purpose. For the static case, forces are time-averaged to obtain mean aerodynamic coefficients, while the data are phase-averaged and low-pass filtered for the second and third cases.

Moreover, dye visualization is used to obtain a qualitative overview of the flow. The apparatus consists of a dye rake made of seven horizontal dye streams that are uniformly distributed over a distance of $2c$, as shown in Fig. 3c. The corresponding streaklines are used here to identify three-dimensional effects.

4 RESULTS

The indirect method is now applied to the different cases described in section 3.1 to calculate the corresponding aerodynamic coefficients. First, the static case is studied using the mean coefficients only. Then, the temporal evolution of the coefficients is determined for the two pitching cases. In order to assess the sensitivity of the results to the choice of the control surface $\mathcal{S}$, all cases are analyzed using seven different control surfaces that differ only by the location of their edge in the wake (i.e., edge $B - C$ in Fig. 1). In

particular, for each surface the edge $B-C$ is moved upstream by a distance $0.06c$ so that the distance between the plate center and that edge ranges from $0.95c$ to $1.3c$, as shown in Fig. 4. The aerodynamic coefficients are then obtained by averaging the results obtained with each of the seven control surfaces. In addition, the standard deviation associated with these different surfaces is also reported.

4.1 Static plate at 30° and 45°

The mean aerodynamic coefficients calculated from Eq. 1 are shown in Tab. 1, together with the mean results obtained from direct force measurement. Note that, due to the time averaging used in this case, the major contribution to the term $\overline{u_i' u_j'}$ stems from the unsteady flow dynamics (i.e., vortex shedding) and not from the turbulence itself. As described above, the standard deviation is computed from the results obtained using different control surfaces $\mathcal{S}$. It measures the sensitivity of the results to the choice of $\mathcal{S}$. The standard deviation associated to the direct force measurements is not shown here since it has a different meaning.

	Indirect calculation		Direct measurement	
AOA	$\overline{c_l}$	$\overline{c_d}$	$\overline{c_l}$	$\overline{c_d}$
30°	1.05 ± 0.01	0.60 ± 0.03	0.97	0.62
45°	1.07 ± 0.01	1.08 ± 0.03	1.07	1.07

Table 1: Mean aerodynamic coefficients computed with the indirect method and obtained from direct measurements for a static plate at 30° and 45° and $\mathrm{Re} = 4 \cdot 10^4$. The standard deviations indicated for the indirect calculation represent the sensitivity of the results to the choice of control surface $\mathcal{S}$.

The results show that the mean drag and lift coefficients are well predicted for both angles of attack. In particular, the largest relative error is found for the lift coefficient at an angle of attack of 30° and amounts to less than 10% . Moreover, the location of the integration path does not seem to impact significantly the results since the standard deviation is low for all cases.

4.2 Small amplitude pitching plate at 30° and 45°

The method is now applied to the small amplitude pitching cases. As mentioned above, the small oscillation imposed to the plate is used to synchronize the PIV system with the shedding in order to perform phase averaging without impacting significantly the flow dynamics.

The evolution of the phase-averaged lift and drag coefficients during a pitching period is shown in Figs. 5 and 6 for the two angles of attack of 30° and 45°, respectively. The coefficients both calculated using the indirect method and directly measured are compared. Similarly to the previous case, the error bars correspond to the standard deviation computed using different control surfaces $\mathcal{S}$. As mentioned in the introduction, the indirect method is very sensitive to the noise in the velocity fields. In order to reduce this noise, the phase-averaged fields are pre-processed, i.e., filtered, by DMD, where only the first three modes are retained to approximate the original fields. These modes correspond here to the mean flow, the shedding/pitching frequency and its first harmonic.

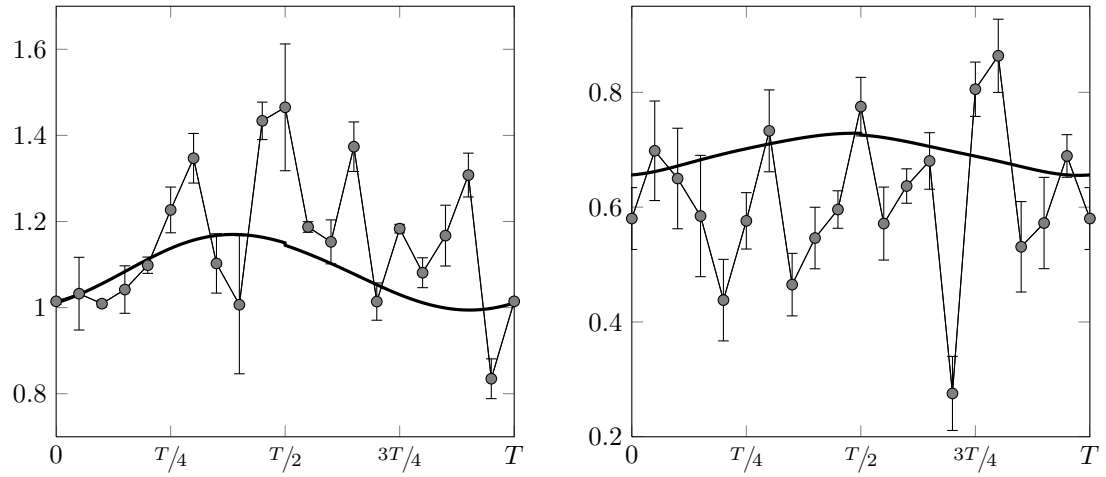

(a) c_l (without DMD) (b) c_d (without DMD)

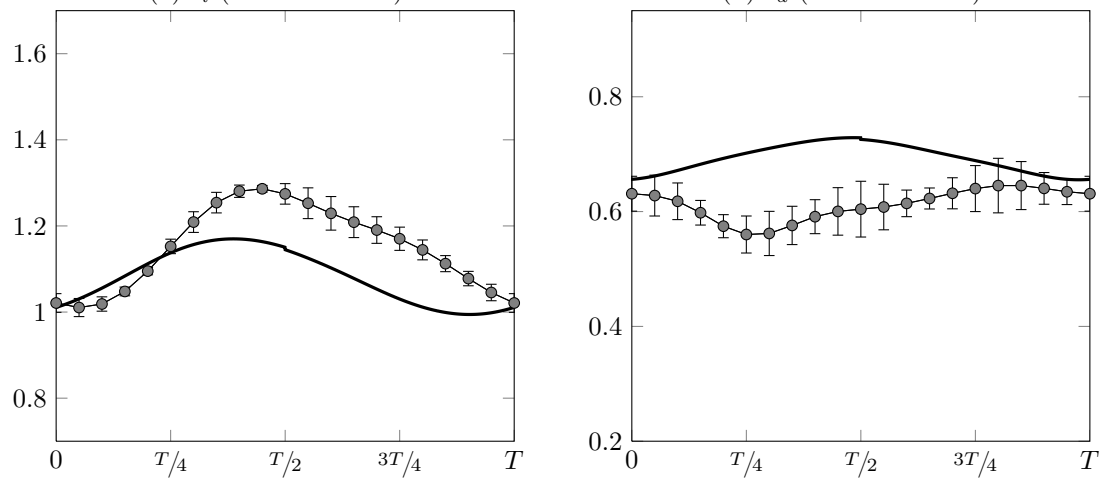

(c) c_l (with 3 DMD modes) (d) c_d (with 3 DMD modes)

Figure 5: Evolution of the lift and drag coefficients within a pitching period for small amplitude plate oscillations around a mean angle of attack of 30° at $\mathrm{Re} = 4 \cdot 10^4$ with and without DMD pre-processing: indirect calculation (symbols) and direct measurements (thick continuous line). The error bars correspond to the sensitivity of the results to the control surface used in the indirect method.

The results are also summarized in Tab. 2, which shows statistics of the lift and drag coefficients. The mean aerodynamic coefficients are obtained by performing an average over the entire period, while the root-mean-square (RMS) values correspond to the deviations from this mean during the period, i.e., it measures the amplitude of the oscillation of the coefficients shown in Figs. 5 and 6 around their mean value.

Although the global trends are captured by the indirect method using the unprocessed fields (see Figs. 5a to 5b and Figs. 6a to 6b), the evolution of the aerodynamic coefficients is very noisy and the results are not meaningful. Additionally, the large error bars indicate a strong sensitivity of the results to the choice of the control surface. These unsatisfactory results can be partially explained by the stitching procedure. Because of the massive flow separation, the flow is three-dimensional and varies strongly from one shedding period to the next, as clearly observed in force measurements and flow visualizations. In particular, while the flow is clearly two-dimensional at 0°, as indicated by Fig. 7a, important three-dimensional structures are observed for this case (Fig. 7b). These effects are less

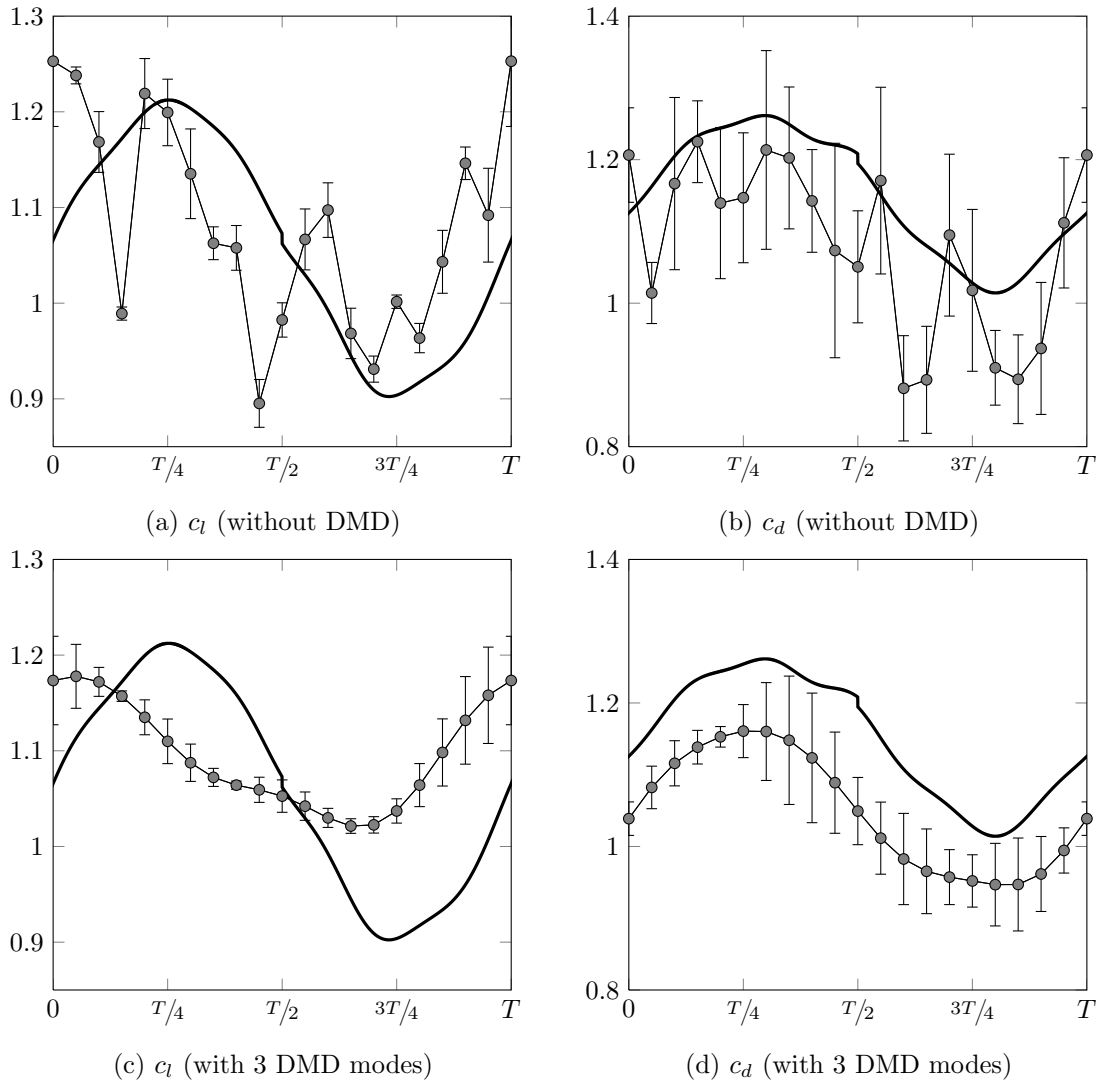

(a) c_l (without DMD)

(b) c_d (without DMD)

(c) c_l (with 3 DMD modes)

(d) c_d (with 3 DMD modes)

Figure 6: Evolution of the lift and drag coefficients within a pitching period for small amplitude plate oscillations around a mean angle of attack of 45° at $\mathrm{Re} = 4 \cdot 10^4$ with and without DMD pre-processing: indirect calculation (symbols) and direct measurements (thick continuous line). The error bars correspond to the sensitivity of the results to the control surface used in the indirect method.

pronounced for the large amplitude case (Fig. 7c) as discussed in next section. As a consequence, the two sets of data for the top and bottom sides of the plate do not match in the overlapping regions. This adds noise to the already existing noise in the velocity fields, which is in turn amplified in the pressure calculation. This problem could be decreased by using a much larger number of samples than presently. Despite this erratic behavior, the mean coefficients are well approximated with a maximum relative error of 12% on the drag, as shown in Tab. 2. The larger RMS values obtained with the indirect method are a direct consequence of the noise in the the temporal evolution of the coefficients.

On the other hand, the pre-processing by DMD leads to much smoother results, as shown by Figs. 5c to 5d and Figs. 6c to 6d and by the lower RMS values in Tab. 2. Nonetheless, several discrepancies can be observed. First, the qualitative evolution of the drag coefficient at 30° is not correctly captured during the first half of the period. A better result is obtained at 45° but with a mean value that is lower than the one obtained by direct

	Indirect calculation				Direct measurement			
AOA	$\overline{c_l}$	c_l^{rms}	$\overline{c_d}$	c_d^{rms}	$\overline{c_l}$	c_l^{rms}	$\overline{c_d}$	c_d^{rms}
30° (without DMD)	1.14	0.15	0.61	0.14	1.08	0.06	0.69	0.02
30° (with 3 DMD modes)	1.14	0.09	0.61	0.03				
45° (without DMD)	1.08	0.10	1.07	0.12	1.06	0.11	1.15	0.09
45° (with 3 DMD modes)	1.10	0.06	1.05	0.08				

Table 2: Mean and RMS values of the lift and drag coefficients for small amplitude plate oscillations around a mean angle of attack of 30° and 45° at Re $= 4 \cdot 10^4$ computed with the indirect method and obtained from direct measurements.

measurement. Secondly, the extrema in the lift coefficient seem to be slightly shifted in phase compared to the force measurements. This shift can also be distinguished in the results based on the unfiltered fields. In addition to the possible causes mentioned above, this phase shift could also be explained by the fact that the indirect method provides the local aerodynamic forces at a section of the plate, while the direct force measurement gives the global forces on the entire span. If the vortex shedding dynamics does not occur simultaneously along the entire span, such a phase shift can be expected between different plate sections, and consequently between a specific section and the spanwise average. This has also been observed in numerical simulations (not shown here). Moreover, since the natural flow dynamics should be as little as possible modified by the pitching motion, the imposed plate oscillation is by design too weak to force a spanwise coherence. Despite these discrepancies the mean aerodynamic coefficients are rather well predicted, as shown in Tab. 2. Finally, note that considering more than three DMD modes does not further improve the results.

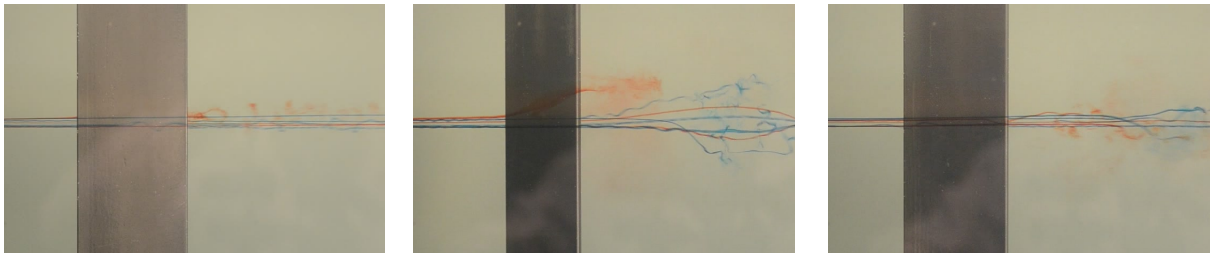

(a) Static at 0° (b) Small amplitude around 45° (c) Large amplitude around 0°

Figure 7: Dye visualization for three cases similar to the ones considered in this study at Re $= 1.8 \cdot 10^4$. Side view: the flow is from left to right and the darker region corresponds to the plate.

4.3 Large amplitude pitching plate

Finally, the method is applied to the large amplitude case. The evolution of the aerodynamic coefficients during a pitching period is shown in Fig. 8 and their statistics are summarized in Tab. 3. In this case, the mean and RMS values are in good agreement with the direct measurements. A much better agreement is also found for the temporal evolution of the lift and drag coefficients compared to the previous case, even without the use of DMD filtering. Nonetheless, small discrepancies are observed for the drag coefficient between $^{3T}/_{8}$ and $^{T}/_{4}$, and between $^{7T}/_{8}$ and T. These two intervals correspond to the motion of vortices across the integration path in the wake, which induces noise during the stitching phase and numerical errors during the pressure integration. This is corroborated

by the large standard deviation observed in these time intervals. This higher sensitivity to the control surface is also observed for the lift coefficient.

The better results found here compared to the previous case can be explained by the higher spanwise coherence of the vortex shedding dynamics driven by the large amplitude oscillations imposed to the plate. Moreover, as mentioned previously, Fig. 7c shows that the three-dimensional effects are reduced, which leads to better phase average statistics. The application of the DMD pre-processing of the velocity fields could further improve the results, which will be done in the future. As previously, the results could also be improved by using a larger number of PIV fields.

	Indirect calculation				Direct measurement			
AOA	$\overline{c_l}$	c_l^{rms}	$\overline{c_d}$	c_d^{rms}	$\overline{c_l}$	c_l^{rms}	$\overline{c_d}$	c_d^{rms}
$0^\circ \pm 30^\circ$	0.02	1.48	0.58	0.44	0.03	1.45	0.55	0.42

Table 3: Mean and RMS values of the lift and drag coefficients for large amplitude plate oscillations around a mean angle of attack of 0° at $\mathrm{Re} = 2 \cdot 10^4$ computed with the indirect method and obtained from direct measurements. The indirectly calculated values are obtained without DMD pre-processing.

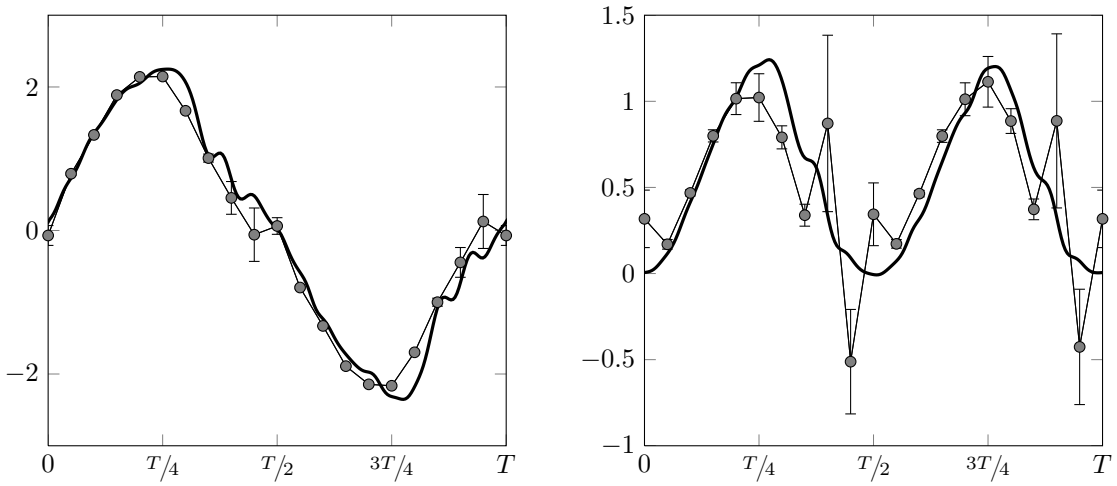

(a) c_l (without DMD) (b) c_d (without DMD)

Figure 8: Evolution of the lift and drag coefficients within a pitching period for large amplitude plate oscillations around a mean angle of attack of 0° at $\mathrm{Re} = 2 \cdot 10^4$ without DMD pre-processing: indirect calculation (symbols) and direct measurements (thick continuous line). The error bars correspond to the sensitivity of the results to the control surface used in the indirect method.

5 CONCLUSIONS AND FUTURE WORK

An indirect method based on the use of the integral formulation of the Navier-Stokes equations has been applied to estimate aerodynamic loads from PIV measurements. The method was selected because of its simplicity and its good behavior in the context of separated flows. This indirect method has been applied to three different unsteady flows around a plate: a static plate at high angle of attack, a small amplitude pitching plate around a high angle of attack and a large amplitude pitching plate around 0°. In order to assess the quality of the indirect calculation, the results have also been compared to direct force measurements.

It has been shown that the mean loads can be estimated with satisfactory accuracy for both static and dynamic cases. However, the time evolution of unsteady coefficients is more difficult to capture. In particular, the level of noise in spatio-temporal data and the stitching procedure impact the calculation of the pressure that is needed to estimate the loads and can in turn produce an erratic time behavior of the solution. This additionally causes a higher sensitivity to the choice of the control surface $\mathcal{S}$.

These problems have been found to be more pronounced in the case of a small pitching motion, for which the flow is found to be more three-dimensional and less periodic. The time evolution is better captured in the case of a large amplitude pitching motion since the strong imposed forcing induce a better spatial and time coherence of the flow. The aerodynamic loads estimated by the indirect method are then in good agreement with direct measurements. It is important to emphasize here that the direct force measurements provide global span-averaged aerodynamic coefficients, while the indirect calculation leads to sectional lift and drag coefficients. If the flow is mostly two-dimensional, both should be equivalent. However, if the flow shows spanwise phase modulations, then the two quantities cannot be directly compared. It is suggested here that the small amplitude pitching motion case, or for that matter the static case, is affected by this three-dimensional flow behavior. The results presented here could thus be closer to reality than suggested by the comparison with direct force measurements.

The noise sensitivity can be strongly reduced through the use of DMD as a pre-processing step. This filters part of the noise and leads to a smoother temporal evolution while keeping the main features of the flow dynamics. It has been applied to the case of a small amplitude pitching plate and led to an improvement in the estimated aerodynamic loads. Nonetheless, discrepancies with direct measurements remained, as the DMD was not able to correct errors introduced by the stitching procedure.

Future work will focus on improving the stitching procedure, which has been shown to have a major impact on the results. Moreover, the DMD pre-processing will be applied to the large amplitude pitching case and the method will be extend to the calculation of the pitching moment coefficient. Finally, a comparison with results obtained with Noca's method will be undertaken.

6 REFERENCES

[1] Noca, F., Shiels, D., and Jeon, D. (1999). A comparison of methods for evaluating time-dependent fluid dynamic forces on bodies, using only velocity fields and their derivatives. *Journal of Fluids and Structures*, 13(5), 551–578.

[2] Albrecht, T., del Campo, V., Weier, T., et al. (2012). Comparison of piv-based methods for airfoil loads evaluation. In *16th International Symposium on Applications of Laser Techniques to Fluid Mechanics, Lisbon, Portugal, July*. pp. 9–12.

[3] Schmid, P. J. (2010). Dynamic mode decomposition of numerical and experimental data. *Journal of Fluid Mechanics*, 656, 5–28.

[4] De Kat, R., Van Oudheusden, B. W., and Scarano, F. (2008). Instantaneous planar pressure field determination around a square-section cylinder based on time resolved stereo-piv. In *Proceedings of the 14th International Symposium on Applications of*

Laser Techniques to Fluid Mechanics, Lisbon, Posrtugal, 07-10 July, 2008, paper No. 1259. Calouste Gulbenkian Foundation.

[5] Lam, K. and Leung, M. (2005). Asymmetric vortex shedding flow past an inclined flat plate at high incidence. *European Journal of Mechanics-B/Fluids*, 24(1), 33–48.

[6] Sterenborg, J., Lindeboom, R., Ferreira, C. S., et al. (2014). Assessment of piv-based unsteady load determination of an airfoil with actuated flap. *Journal of Fluids and Structures*, 45, 79–95.

[7] Vandenheede, R., Bernal, L. P., Morrison, C. L., et al. (2012). Parameter space exploration of bio-inspired hover kinematics. In *42nd AIAA Fluid Dynamics Conference and Exhibit, New Orleans, USA, 25-28 June 2012; AIAA 2012-3155*. American Institute of Aeronautics and Astronautics (AIAA).

[8] Baik, Y. S., Bernal, L. P., Granlund, K., et al. (2012). Unsteady force generation and vortex dynamics of pitching and plunging aerofoils. *Journal of Fluid Mechanics*, 709, 37–68.

COPYRIGHT STATEMENT